2015 ASIA-PACIFIC SOLAR RESEARCH CONFERENCE

Peer Reviewed
2015 Solar Research Conference

Xiang Gao

Structural Performance of Micro and Nano-structured Ceria for Solar Thermochemical Fuel Production

Xiang Gao[1], Alejandro Vidal[1], Alicia Bayon[2], Roman Bader[1], Jim Hinkley[2], Wojciech Lipiński[1], Antonio Tricoli[1]

[1]*Research School of Engineering, the Australian National University, Canberra ACT 2601, Australia*

[2]*CSIRO Energy Technology, P. O. Box 330, Newcastle, NSW 2300, Australia*

E-mail: Michael.gao@anu.edu.au

Abstract

Flame-made nano-structured and commercial micro-structured ceria powders are assessed for two-step carbon dioxide splitting (CDS) driven by a reduction step of methane partial oxidation (MPO). The MPO and CDS reaction rates are strongly dependent on the structural properties of the ceria powders. The nano-structured material shows up to 167% and 144% higher H_2 and CO average production rates during MPO, respectively, and 97% higher CO average production rate during CDS than the micro-structured commercial ceria. After 10 consecutive cycles, the rates are still 57%, 54% and 15% higher, respectively. The higher reaction rates for the nano-structured ceria are attributed to the initially 10 times higher specific surface area of the flame-made nano-structured ceria (76.6 m^2g^{-1}) than that of commercial micro-structured powders (7.3 m^2g^{-1}). These findings indicate that thermal and chemical stabilization of nano-scale structural features is the key to achieving long-term cyclability of ceria in high temperature solar thermochemical fuel production.

1. Introduction

Solar production of fuels via high-temperature thermochemical processing is a promising approach to the chemical storage of solar energy for stationary and mobile applications. An industrially viable process is the solar production of synthesis gas (syngas), a mixture of hydrogen and carbon monoxide. Syngas can be directly used for efficient power generation via gas power cycles, or further transformed into hydrocarbon fuels or carbonaceous commodity materials via synthesis processes such as Fischer–Tropsch and methanation.

Two-step thermochemical metal-oxide redox cycles have been demonstrated as an efficient pathway for hydrogen and carbon monoxide production via water (WS) and carbon dioxide (CDS) splitting, respectively. A desired stoichiometric ratio H_2:CO in the syngas is achieved through controlled mixing of the products of WS and CDS cycles. Conventional two-step redox cycles rely on the direct thermal reduction of metal oxides. This approach requires high operating temperatures, typically above 1673 K, and low oxygen partial pressures (Bader et al., 2013). However, high process temperature requires sophisticated reactor designs and materials to maintain reactor durability and acceptable thermal losses. Furthermore, the overall process efficiency is negatively affected by the requirement of large quantities of inert sweep gas (Bader et al., 2013). An alternative approach, reduction under vacuum, requires mechanical energy input and is challenging for implementation at the high operating reactor temperatures. Yet another alternative approach is to employ a carbothermal reduction process

of a metal oxide with a carbonaceous reducing agent such as the methane partial oxidation (MPO). A thermodynamic study performed by Krenzke and Davidson (Krenzke and Davidson, 2014) suggested that coupling MPO to the reduction step of the solar ceria redox cycle enables production of high-quality syngas. The predicted solar-to-fuel efficiencies are 39% and 40% for the CDS and WS step, respectively, without accounting for additional heat recovery. The carbothermal CDS/WS cycles, in particular with MPO, are considered as a short- to mid-term strategy for solar fuel production.

A large number of metal-oxide redox systems have been investigated for the production of syngas by MPO-CDS/WS cycles including Fe_3O_4/FeO, Cu(II)-ferrites (Kang et al., 2008), Ni(II)-, Zn(II)-, and Co(II)-ferrites (Kodama et al., 2002), WO_3/W (Kodama et al., 2000), $CeO_2/CeO_{2-\delta}$ (Otsuka et al., 1998), $La_{1-x}Sr_xFeO_3$ perovskites (Evdou et al., 2010), and $LaNi_{1-x}Co_xO_3$ perovskites (Silva et al., 2011). CeO_2 has attracted some particular attention as it offers faster kinetics and more enhanced long-term stability than other metal oxides. The MPO-CDS/WS two-step solar thermochemical redox cycle of CeO_2 is written as:

1st, endothermic step:

$$CeO_2 + \delta CH_4 \rightarrow CeO_{2-\delta} + \delta CO + 2\delta H_2, \Delta H^{o}_{298K} = +166.23 \text{kJ mol}^{-1} \quad (1)$$

2nd, exothermic step:

$$CeO_{2-\delta} + \delta CO_2 \rightarrow CeO_2 + \delta CO, \Delta H^{o}_{298K} = -22.09 \text{kJ mol}^{-1} \quad (2a)$$

and/or

$$CeO_{2-\delta} + \delta H_2O \rightarrow CeO_2 + \delta H_2, \Delta H^{o}_{298K} = -63.29 \text{kJ mol}^{-1} \quad (2b)$$

During the first step ceria is reduced by CH_4 with a net change in oxygen stoichiometry of δ. No phase change occurs during the reduction as ceria is able to accommodate substantial release of lattice oxygen ($\delta < 0.25$ at 1273 K) while maintaining a stable cubic crystal phase (Chueh and Haile, 2010). In the second step ceria reacts with CO_2 or H_2O reincorporating up to δ of oxygen into the lattice. Both steps can be run isothermally in the temperature range of 873–1273 K.

This (1)–(2) cycle has been experimentally demonstrated with pure ceria. Several ceria-based mixed oxides have been tested to improve the cyclic performance including CeO_2-ZrO_2 (Otsuka et al., 1999), CeO_2-FeO_2 (Li et al., 2010), and WO_3-CeO_2-ZrO_2 (Sim et al., 2010). Morphology studies of pure ceria including specific surface area and porosity has also been shown to significantly improve peak fuel production rates by up to 175% for two-step thermochemical metal-oxide redox cycles with direct thermal reduction under inert gas (Venstrom et al., 2012). Flame synthesis was employed to produce pure CeO_2 with high specific surface area and crystallinity (Mädler et al., 2002). Flame-made ceria nanoparticles were demonstrated by Stark et al. (Stark et al., 2005) to improve thermal stability and oxygen exchange capacity. However, studies on improving thermochemical performance of pure ceria in MPO-WS/CDS cycling by introducing nano-scale structural features are not reported in literature.

Here, we report on the performance of micro- and nano-scale structured pure ceria for solar fuel production via two-step MPO-CDS thermochemical redox cycles. The performance of commercial micro-structured and flame-made nano-structured ceria is evaluated comparatively using an IR furnace setup with a vertical-tube packed-bed reactor. The

performance metrics are the instantaneous and total amounts of H_2 and CO produced during isothermal MPO-CDS cycling at 1173 K. The structural changes of ceria samples during 10 testing cycles are evaluated by characterising crystal size, specific surface area and TEM morphology before and after cycling.

2. Experimental

2.1 Material synthesis

To synthesize nano-structured ceria particles using flame spray pyrolysis, cerium (III) acetate hydrate (Alfa Aesar, 99.995%) is dissolved in a 2-ethylhexanoic acid (SAFC, purity >99%) heated with 368 K oil bath to prepare the combustible liquid solution. Next, xylene of the volume equal to that of the 2-ethylhexanoic acid is added to the solution to reach a total Ce-atom concentration of 0.2 mol L^{-1}. The solution is fed at 5 mL min^{-1} rate through a custom built nozzle (Nasiri et al., 2015), and atomized with an oxygen flow of 5 L min^{-1} (COREGAS grade 2.5) with a pressure drop of 4 bar. The resulting spray is ignited with a surrounding annular premixed methane ($CH_{4\text{-flamlet}}$, flow rate of 1.2 L min^{-1}, COREGAS grade 4.5) and oxygen ($O_{2\text{-flamlet}}$, flow rate of 2 L min^{-1}, COREGAS grade 2.5) flame. Nanoparticle powders are collected with a vacuum pump (ICME Type M80B4) on water-cooled glass-fiber filters (Sartorius glass microfiber, 160-mm diameter) placed at 38 cm height above burner (HAB). This material is referred to in the following text as nano-structured ceria.

Commercially available ceria micro-structured powders (Alfa Aesar, 99.9%) are used in this study as an alternative material for the purpose of comparative evaluation of thermochemical performance in syngas production. This material is referred to in the following text as micro-structured ceria.

2.2 Material characterization

Samples of micro and nano-structured ceria are characterized by X-ray diffraction (XRD, D2 phaser diffractometer, Bruker). Each sample powder is scanned using Cu Kα (1.54 Å) radiation source with an operating voltage and current of 30 kV and 10 mA, respectively. The scan rate of 0.75° min^{-1} is applied to record the XRD patterns in the range of 10–80° at an increment of 0.02°. The Scherrer equation is applied for the most intense peak to determine the crystal size. The Brunauer–Emmett–Teller (BET) specific surface area is measured by N_2 adsorption–desorption isotherms at 77 K, using a surface and porosity analyser (TriStar II, Micromeritics). The samples are degassed at 623 K for 4 hours prior to measurement. The samples are also analysed using transmission electron microscopy (TEM, Hitachi H7100FA, operated at 125 kV). Specimens are dispersed in ethanol (200 proof, Sigma Aldrich) and sonicated for 1 h at 318 K and 60 W (1.5 L capacity) before deposited on 200-mesh holey carbon filmed copper grids.

2.3 Reaction testing

The cyclic syngas production performance of the ceria samples is investigated in a vertical-tube reactor placed inside an electric IR furnace (P4C-VHT, Advance Riko) depicted in Figure 1. The powder samples are sandwiched between two 2-mm thick highly-porous and temperature-resistant alumina wool disks, located on-axis of an alumina tube. The ceria sample thickness is varied between 1 mm and 2 mm which allows for a nearly-uniform temperature distribution in the sample. The inner diameter and wall thickness of the tube are 12.5 mm and 3 mm, respectively. The tube is placed in the centre of the furnace and enveloped by a quartz tube for protection of IR lamps against thermal degradation. The tube is sealed to stainless steel connectors with Kalrez O-rings, and closed with mechanic valves (Swagelok) at both ends. Gas mixtures are regulated by mass flow controllers (Bronkhorst)

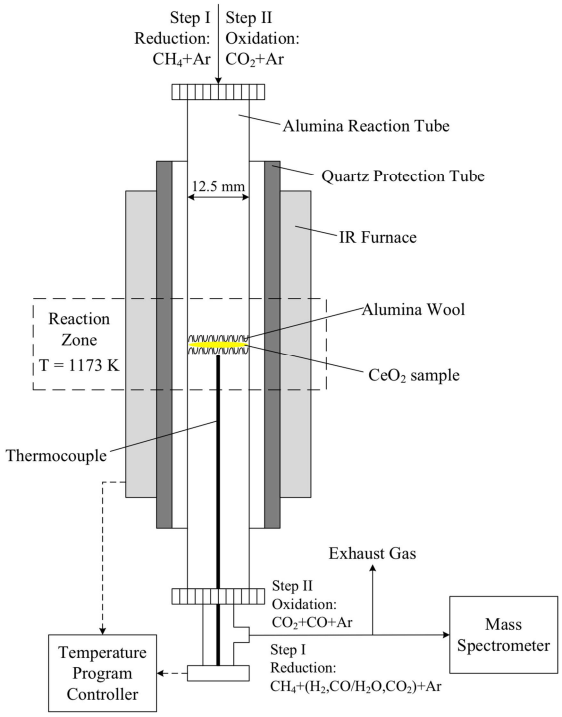

Figure 1. Schematic of the experimental setup for the two-step MPO-CDS cycling

before delivered through the top of the tube. Sample temperature is measured using a type-K thermocouple inside the alumina tube. The composition of the effluent gases is continuously monitored by a quadrupole mass spectrometer (OmniStar^{TM} GSD 320, Pfeiffer Vacuum). All the monitored gas components are calibrated in the mass spectrometer using standard mixtures of the individual solute (CH_4, CO_2, and CO/H_2) in a reference Ar gas. All gas volumes are reported at 293 K and 1 atm. The average production rates of H_2 and CO are calculated over the 2-100% peak production rate time period.

The operating temperature for isothermal MPO-CDS ceria redox cycles, 1173K, is derived from thermodynamic analysis (Krenzke and Davidson, 2014) and has been experimentally evaluated (not shown in this study) to produce H_2 and CO at a close 2:1 ratio while maintaining sufficiently fast reaction kinetics.

To simulate the operation conditions of a solar reactor, a discontinuous two-day testing was conducted for both samples performing a total of 10 cycles (divided into 4 and 6 cycles in the two testing days). In each testing day, the tubular reactor was initially purged of air under a 250 mL min^{-1} flow of pure Ar (COREGAS grade 5.0). The reactor was then heated from 293 K to 1173 K at a ramp of 80 K min^{-1}. Subsequently, the sample was cyclically reduced and oxidized with CH_4 (COREGAS grade 4.5) and CO_2 (COREGAS grade 4.5). The reduction step was performed using a mixture of CH_4 in Ar (8 vol% CH_4) at a total flow rate of 250 mL min^{-1}. The sample was allowed to reduce for 30 min. Between the cycle steps and the cycles, the tube was purged with Ar (250 mL min^{-1}) for 15 min. The oxidation was then initiated by delivering a mixture of CO_2 in Ar (4 vol% CO_2) at a total flow rate of 250 mL min^{-1}. Each oxidation step was allowed for 15 min. The time required for the reduction and oxidation steps was determined by preliminary tests and was sufficient for both samples to complete the reaction until no further fuel production could be detected from the mass spectrometer. At the end of each testing day, the reactor was cooled to 293 K at 80 K min^{-1} using an external cooling system and under Ar purge gas. Once the sample reached room temperature, the valves at both ends of the alumina tube were closed, and the samples were preserved in the Ar atmosphere between the testing days.

Table 1. Physical and chemical properties of the commercial and flame-made CeO_2

Material	SSA (m^2 g^{-1})		d_{BET} (nm)		d_{XRD} (nm)	
	As-Prepared	10 cycles	As-Prepared	10 cycles	As-Prepared	10 cycles
Micro- CeO_2	7.34	1.59	106.9	493.3	83.8	86.1
Nano- CeO_2	76.63	1.58	10.2	496.4	9.4	51.3

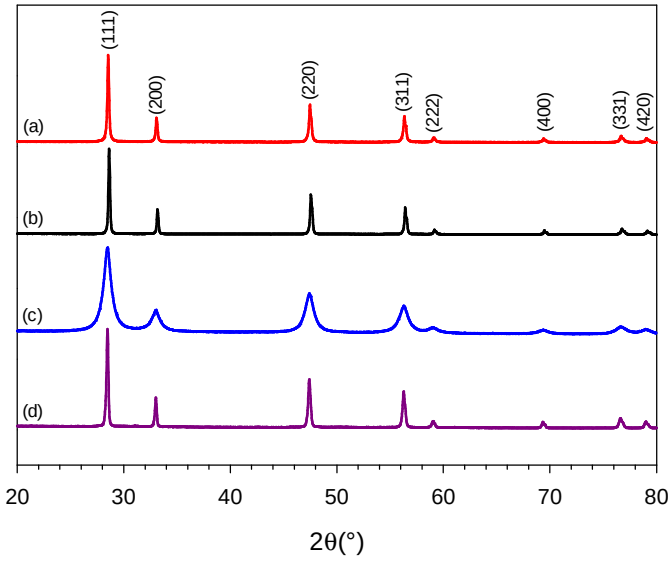

Figure 2. XRD patterns of the commercial micro-structured and flame-made nano-structured ceria powders: (a) micro-structured before cycling, (b) micro-structured after cycling, (c) nano-structured before cycling, (d) nano-structured after cycling.

3. Results and discussion

The results of the nitrogen adsorption–desorption and XRD crystal size measurements are summarized in Table 1. The XRD spectra are displayed in Figure 2 and correspond to the spectra of cubic ceria (JCPDS No. 34-0394) with a displacement of 0.009°. The most intense peak was located at 28.540°, and the average crystal size of micro-structured ceria increased from 83.8 nm (as-prepared) to 86.1 nm after 10 MPO-CDS cycles (Table 1). The nano-structured ceria consists of 9.4 nm crystals in diameter and grow to 51.3 nm after 10 MPO-CDS cycles (Table 1). These results show that the size of the crystals of the micro-structured powder remains nearly constant during thermochemical cycling. The crystals size of the nanostructured ceria, on the contrary, increases by a factor of 5.

The as-prepared BET surface area of the micro-structured ceria was 7.34 m^2 g^{-1} and decreased to 1.59 m^2 g^{-1} after the 10 MPO-CDS thermal cycles (Table 1). Although, for these commercial samples a similar irregular faceted shape is observed before and after cycling, the decrease in surface area can still be associated with changes in the grain TEM morphology a fractal-like and disordered morphology constituted by partially sintered nanoparticle agglomerates. After the 10 MPO-CDS cycles, the specific surface area of nano-structured ceria decreased by 98%. Figure 3d confirms that the nano-structured ceria experienced

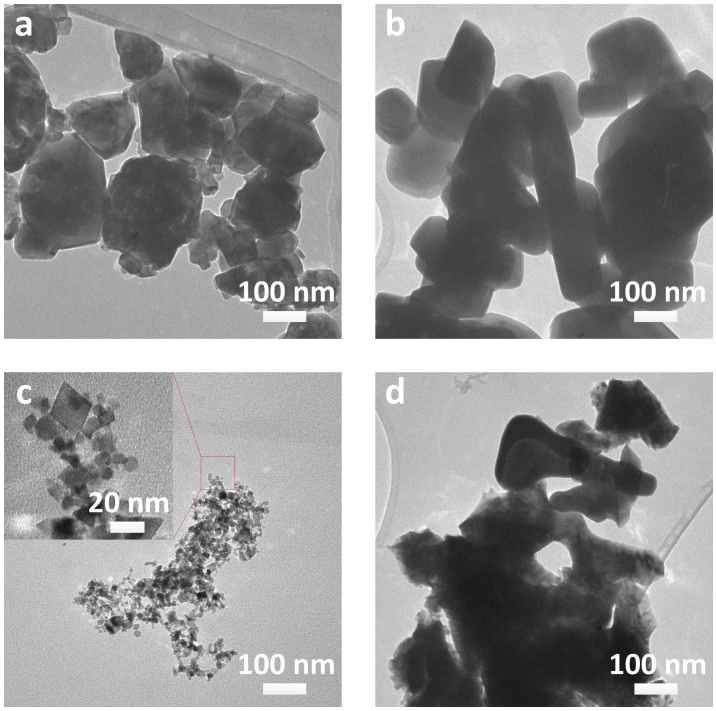

Figure 3. TEM micrographs of the micro-structured and nano-structured ceria powders: (a) micro-structured before cycling, (b) micro-structured after cycling, (c) nano-structured before cycling, (d) nano-structured after cycling.

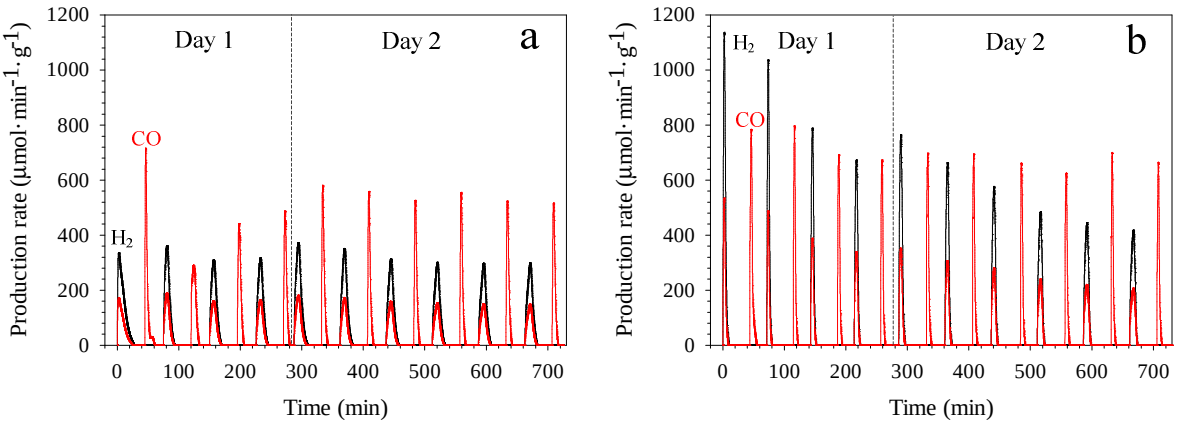

Figure 4. H_2 and CO production rates during thermal cycling for (a) the micro-structured and (b) the nano-structured ceria powders.

significant sintering after cyclic thermochemical reactions and prolonged residence time at high temperatures. Nano-structured ceria particles have a higher potential to cluster and agglomerate to minimize the surface energy than micro-structured ceria, hence more severe sintering is expected.

Figure 4 shows the H_2 (MPO), CO (MPO), and CO (CDS) production rates of the micro and nano-structured ceria as a function of time during an exemplary 10 MPO-CDS cycles experiment. During the MPO reduction step, CO and H_2 are produced immediately after the introduction of CH_4. Their production rates increase very fast, reaching a maximum in 3 to 5 minutes, and then the production rates decay. This is tentatively attributed to the combined effects of solid-state diffusion of oxygen and deposition of carbon. Upon depletion of the ceria surface oxygen, solid-state diffusion of O_2 from the lattice becomes the rate-limiting step for the MPO reaction.

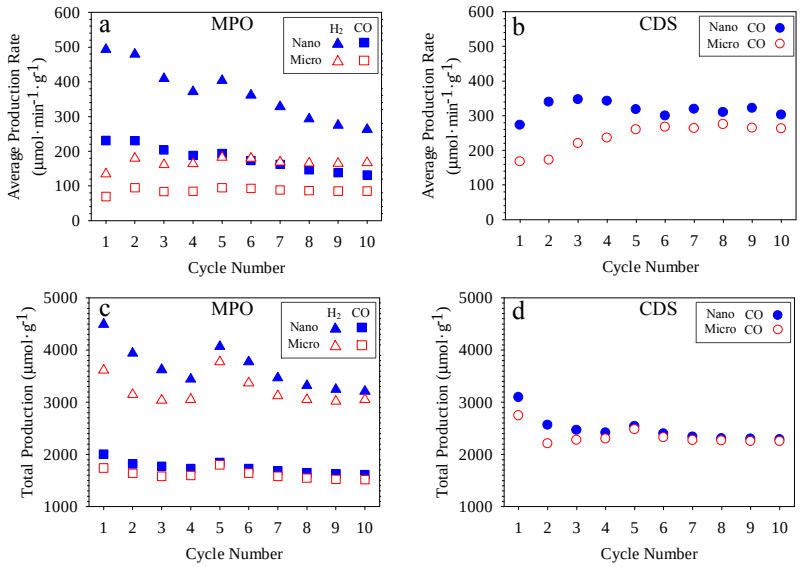

Figure 5. Average production rates (a, b) and total amount produced (c, d) of H_2 (MPO), CO (MPO) and CO (CDS) for micro-structured and nano-structured powders.

Similar production rates profiles are also observed during the CDS oxidation steps. However, the pronounced spike in CO production rate during the first oxidation step of the micro-structured ceria (Figure 4a) is unexpected. This is tentatively attributed to the volatilisation of organic impurities at high temperature that may have been present on the commercial ceria surface. Thus, the results of the second cycle are used to evaluate initial peak production performance. Specifically, micro-structured ceria achieved peak production rates of 362.0 µmol min^{-1} g^{-1}, 190.1 µmol min^{-1} g^{-1} and 291.1 µmol min^{-1} g^{-1} for H_2 (MPO), CO (MPO) and CO (CDS), respectively. For the nano-structured ceria, the corresponding rates are 1038.1 µmol min^{-1} g^{-1}, 489.2 µmol min^{-1} g^{-1} and 798.7 µmol min^{-1} g^{-1}, which constitute increases of 187%, 157% and 174%, respectively.

Figure 5a and b show the average H_2 and CO production rates of the micro-structured and nano-structured ceria powders. In the second cycle (Figure 5a and b), during MPO the nano-structured ceria had 167% and 144% higher average H_2 and CO production rates, respectively, and during the CDS 97% higher average CO production rate than the micro-structured ceria. In the 10th cycle, these results are still 57%, 54% and 15% faster, respectively. This suggests that the nano-structured ceria still reduces and oxidises significantly faster than commercial ceria even after 11 hours of accumulated MPO-CDS cycling.

In Figure 5a, it is noticeable that while the production rates of micro-structured ceria remained relatively stable throughout the cycles, the CO and H_2 production rates of the nano-structured ceria declined by more than 40% and have nearly converged to a constant performance only after 10 cycles. This is in line with Figure 4b that suggests a declining trend of peak production rates for nano-structured sample during reduction, while the lower rates of micro-structured ceria remained relatively stable (Figure 4a). This is attributed to the significantly higher sintering of the nano-structured ceria, which drastically reduces the surface area available for the MPO and CDS reactions. Therefore, in order to maintain the superior initial performance of the flame-made ceria, the high specific surface area of the flame-made ceria must to be maintained.

Figure 5c and d show the total production of H_2 and CO per MPO and CDS cycle. The average amounts of H_2 (MPO), CO (MPO) and CO (CDS) produced over 10 MPO-CDS cycles are 3224.2 µmol g^{-1}, 1617.5 µmol g^{-1}, and 2337.3 µmol g^{-1} for the micro-structured

ceria, and 3659.4 µmol g^{-1}, 1748.3 µmol g^{-1}, and 2470.0 µmol g^{-1} for the nano-structured ceria. While nano-structured ceria leads to significantly higher CO and H_2 production rates compared to micro-structured ceria, the amounts of CO and H_2 produced per cycle are comparable. The averaged production rates were obtained over the time periods with an H_2 and CO production rate above 2% of the maximum production rates for each single MPO and CDS step (as explained in section 2.3). These time periods vary slightly but are consistently shorter than the total step time (30 min for MPO and 15 min for CDS). This is also visible in Figure 4, where all reactions finish before the total step time, and the nano-structured ceria finishes much faster than micro-structured ceria. As a consequence, even though the total productions between the two structured ceria do not show much difference, this is due to the very large step times. Notably, the nano-structured ceria completes the redox reactions in significantly shorter time than the micro-structured ceria and can be operated with much shorter step times.

According to experimental studies (Otsuka et al., 1998), at an isothermal temperature of 973 K, the H_2 and CO production during the MPO reduction step using commercially available ceria were approximately 730 µmol g^{-1} at 8.5 µmol min^{-1} g^{-1} and 339 µmol g^{-1} at 3.0 µmol min^{-1} g^{-1}, respectively. These values are comparable to the results obtained here with the micro-structured ceria considering the more favourable experimental conditions such as higher operating temperatures, higher feed gas flow rates, and targeted structural enhancement that improve the overall MPO reaction performance. In terms of the amount of CO produced during the CDS oxidation step, here we have observed significant improvement with both micro and nano-structured ceria over that reported for the inert gas reduction (IGR) process (Chueh et al., 2010; Furler et al., 2012). Specifically in these works, at an isothermal temperature of 1073–1200 K, following the IGR reduction, the CDS oxidation step resulted in only 455±215 µmol g^{-1} of CO or H_2, with average production rates at 45.5±29.5 µmol min^{-1} g^{-1}. Notably, here, the amount of CO produced during the CDS oxidation step is ca 5 times higher (2403.5±66.5 µmol g^{-1}) with a 6 times higher average production rate of 267.5±100.5 µmol $min^{-1}g^{-1}$. Theoretical analysis (Bader et al., 2013) has suggested that at 1773 K conventional IGR is only capable to provide a change in stoichiometry for ceria of 0.06. By using the MPO for the reduction step, the obtainable reduction in stoichiometry is significantly increased. Further analysis shows that a stoichiometry variation of 0.2693±0.0076 was achieved in this study. Compared to theoretical thermodynamic calculations indicating a maximal stoichiometry variation of 0.25 for the MPO reduction of the cubic fluorite crystal structure of ceria (Krenzke and Davidson, 2014), the values obtained in this work is comparable and only slightly exceeding this limit. Further in-situ characterisation is required to determine if other crystalline phases are formed during the reduction step.

The reaction stoichiometry in equation (1) and (2a) indicates a H_2:CO product ratio in the MPO step of 2:1. The total production of CO in the CDS step should be equal to that in the MPO step. However, according to the measured total productions (Figure 5c and d), the H_2 to CO ratio in the MPO steps is larger than 2. Furthermore, the total CO production in the CDS step is larger than the total CO production in the MPO step. We attribute these results to formation of some carbon during the MPO step. In fact, thermal cracking of CH_4 during MPO can produce solid carbon and H_2. During CDS this carbon can be oxidized by CO_2, resulting in additional CO production.

Figure 5c and d show that the total fuel production for the micro-structured and nano-structured ceria converge to 3132.1±113.6 µmol g^{-1}, 1570.5±58.1 µmol g^{-1}, and 2271.4±23.3 µmol g^{-1} for H_2 (MPO), CO (MPO) and CO (CDS), respectively. This suggests limited effects of the structural features on the solid-state redox equilibrium of ceria. This is also confirmed

by evaluating the stoichiometry of the last cycle between the micro-structured and nano-structured ceria, in contrast to the drastic difference of 15–57% in average production rates, the achieved stoichiometry variation from flame-made nano-structured ceria (0.2769±0.0007) is only 5–7% higher than that of commercial micro-structured ceria (0.2617±0.0006). This indicates that while structural properties of ceria influence the kinetics of fuel production, its influence on the chemical equilibrium of the system is limited.

4. Conclusion

This study investigated the impact of nano-scale structural features of pure ceria on its syngas production performance during two-step MPO-CDS isothermal redox cycles. Specifically, production rates and total amount of produced H_2 and CO in each cycle for the micro and nano-structured ceria samples are comparatively evaluated and analysed with respect to the evolution of their key structural parameters such as specific surface area, crystal size and TEM morphology.

Initially, the reaction rates of flame-made nano-structured ceria are at least 97% higher than the micro-structured commercial ceria during the MPO-CDS cycles at 1173 K isothermal redox conditions. Even after 10 cycles, the nano-structured ceria has still at least 15% faster reaction rates compared with micro-structured ceria. This is attributed to its initial higher specific surface area of 76.63 m^2 g^{-1} that accelerate the solid-state O_2 diffusion kinetic. The potential of nano-structured ceria to benefit the kinetics of syngas production is suggested.

While the initial syngas production rates of the nano-structured ceria are the highest among those reported in literature, the rates decline by more than 40% after 10 cycles. The rapid deterioration of the activity of nano-structured ceria suggests that the ability to maintain the structural features in the material is crucial for long-term solar thermochemical fuel production. Hence, a research challenge is to find means to avoid sintering of such fine nano-scale structural features during long-term exposure to a high temperature reducing environment. Based on the TEM images, the as-synthesized flame-made nano-structured ceria presents agglomerated individual nanoparticles. These particles are prone to form necking with adjacent particles at high operating temperatures and initiate further sintering (Tricoli et al., 2008). From this perspective, future studies will examine feasible options for optimizing the nano-structures of ceria, in order to retain the very high initial reaction rates.

References

Bader, R., Venstrom, L. J., Davidson, J. H., and Lipiński, W., 2013, 'Thermodynamic analysis of isothermal redox cycling of ceria for solar fuel production', *Energy & Fuels*, 27, p5533–5544.

Chueh, W. C., Falter, C., Abbott, M., Scipio, D., Furler, P., Haile, S. M., and Steinfeld, A., 2010, 'High-Flux Solar-Driven Thermochemical Dissociation of CO_2 and H_2O Using Nonstoichiometric Ceria', *Science*, 330, p1797–1801.

Chueh, W. C., and Haile, S. M., 2010, 'A thermochemical study of ceria: exploiting an old material for new modes of energy conversion and CO_2 mitigation', *Philos Trans A Math Phys Eng Sci*, 368, p3269–3294.

Evdou, A., Zaspalis, V., and Nalbandian, L., 2010, '$La_{1-x}Sr_xFeO_{3-\delta}$ perovskites as redox materials for application in a membrane reactor for simultaneous production of pure hydrogen and synthesis gas', *Fuel*, 89, p1265–1273.

Furler, P., Scheffe, J.R., and Steinfeld, A., 2012, 'Syngas production by simultaneous splitting of H_2O and CO_2 via ceria redox reactions in a high-temperature solar reactor', *Energy & Environmental Science*, 5, p6098–6103.

Kang, K.S., Kim, C.H., Cho, W.C., Bae, K.K., Woo, S.W., and Park, C.S., 2008, 'Reduction characteristics of $CuFe_2O_4$ and Fe_3O_4 by methane; $CuFe_2O_4$ as an oxidant for two-step thermochemical methane reforming', *International Journal of hydrogen energy*, 33, p4560–4568.

Kodama, T., Ohtake, H., Matsumoto, S., Aoki, A., Shimizu, T., and Kitayama, Y., 2000, 'Thermochemical methane reforming using a reactive WO_3/W redox system', *Energy*, 25, p411–425.

Kodama, T., Shimizu, T., Satoh, T., Nakata, M., and Shimizu, K.I., 2002, 'Stepwise production of CO-rich syngas and hydrogen via solar methane reforming by using a Ni (II)–ferrite redox system', *Solar Energy*, 73, p363–374.

Krenzke, P. T., and Davidson, J. H., 2014, 'Thermodynamic analysis of syngas production via the solar thermochemical cerium oxide redox cycle with methane-driven reduction', *Energy & Fuels*, 28, p4088–4095.

Li, K., Wang, H., Wei, Y., and Yan, D., 2010, 'Syngas production from methane and air via a redox process using Ce–Fe mixed oxides as oxygen carriers', *Applied Catalysis B: Environmental*, 97, p361–372.

Mädler, L., Stark, W. J., and Pratsinis, S. E., 2002, 'Flame-made ceria nanoparticles', *Journal of Materials Research*, 17, p1356–1362.

Nasiri, N., Bo, R., Wang, F., Fu, L., and Tricoli, A., 2015, 'Ultraporous Electron-Depleted ZnO Nanoparticle Networks for Highly Sensitive Portable Visible-Blind UV Photodetectors' *Advanced Materials*, 27, p4336–4343.

Otsuka, K., Wang, Y., and Nakamura, M., 1999, 'Direct conversion of methane to synthesis gas through gas–solid reaction using CeO_2–ZrO_2 solid solution at moderate temperature', *Applied Catalysis A: General*, 183, p317–324.

Otsuka, K., Wang, Y., Sunada, E., and Yamanaka, I., 1998, 'Direct partial oxidation of methane to synthesis gas by cerium oxide', *Journal of Catalysis*, 175, p152–160.

Silva, C.R., da Conceição, L., Ribeiro, N.F., and Souza, M.M., 2011, 'Partial oxidation of methane over Ni–Co perovskite catalysts', *Catalysis Communications*, 12, p665–668.

Sim, A., Cant, N.W., and Trimm, D.L., 2010, 'Ceria–zirconia stabilised tungsten oxides for the production of hydrogen by the methane–water redox cycle', *International Journal of Hydrogen Energy*, 35, p8953–8961.

Stark, W. J., Grunwaldt, J.D., Maciejewski, M., Pratsinis, S.E., and Baiker, A., 2005, 'Flame-made Pt/ceria/zirconia for low-temperature oxygen exchange', *Chemistry of materials*, 17, p3352–3358.

Tricoli, A., Graf, M., and Pratsinis, S. E., 2008, 'Optimal doping for enhanced SnO_2 sensitivity and thermal stability' *Advanced Functional Materials*, 18, p1969–1976.

Venstrom, L. J., Petkovich, N., Rudisill, S., Stein, A., and Davidson, J. H., 2012, 'The effects of morphology on the oxidation of ceria by water and carbon dioxide', *Journal of Solar Energy Engineering*, 134, 011005.

Acknowledgements

This research was funded in part by the Australian Solar Thermal Research Initiative (ASTRI) through the Australian Renewable Energy Agency (ARENA). The financial support by the ARC APA (X. Gao), the ARC Future Fellowship (W. Lipiński), and the ARC Discovery Project DP150101939 (A. Tricoli) are gratefully acknowledged.